Crystal-Phase Engineering of PdCu Nanoparticles for Catalytic Reduction of NO by CO

Shuang Liu, Yong Li, Yuemin Wang, and Wenjie Shen*

ABSTRACT: Tuning the crystal phase of bimetallic nanoparticles has emerged as a promising strategy to boost their catalytic performance, but identifying the active site at the single-nanoparticle scale is rarely done and remains challenging. Here, the crystal phase of a PdCu single nanoparticle, spatially confined by a silica shell, was mediated between the ordered body-centered cubic (B2) phase and the disordered face-centered cubic (A1) phase. During the crystal-phase transition, the porous silica shell prevented the bimetallic nanoparticles from sintering under reactive gases and at elevated temperatures, enabling us to alter the crystal phase while keeping the particle size and atomic composition unchanged. Combined microscopic and spectroscopic characterizations revealed that the B2 particle was enclosed predominantly by the {110} facets over which Pd and Cu atoms were populated alternatively, while the A1 particle exposed mainly the {111} facets terminated by a random distribution of Pd and Cu atoms. When applied to catalyze NO reduction by CO, the B2 particle showed a much higher activity with a reaction rate of 4.5 times greater than that of the A1 particle. It was proposed that the orderly arranged Pd and Cu atoms on the {110} facets, exposed by the B2 particle, favored the coadsorption of NO and CO and further facilitated the dissociation of NO as the rate-determining step in the reaction network.

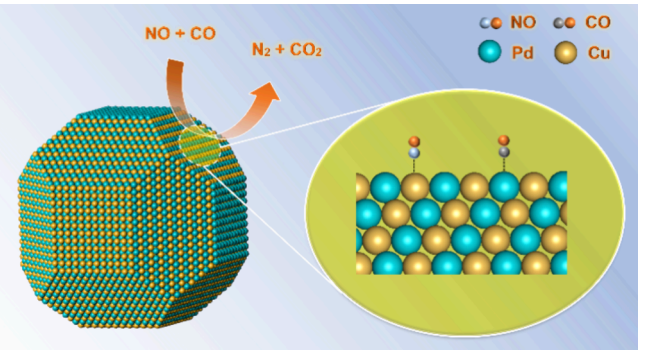

1. INTRODUCTION

Crystal-phase engineering of bimetallic nanoparticles enables modulation of the geometric and electronic structure of the surface atoms and would in turn alter their catalytic property. PdCu nanoparticles crystallize in the disordered face-centered cubic (fcc, A1) phase or the ordered body-centered cubic (bcc, B2) structure, depending on the arrangement of Pd and Cu atoms in the lattice cell. The ordered B2 phase often outperformed the disordered A1 phase in electrocatalytic conversion of small molecules.[1−9] For instance, the activity of the B2-PdCu particles was two times greater than that of the A1-PdCu particles for electrochemical reduction of N_2 to ammonia.[4] The stronger d−d coupling effect between Pd−Cu sites in the B2 structure favored electron transfer from PdCu to N_2. For electrochemical reduction of nitrate, the B2-PdCu particles exhibited pronounced nitrate conversion (94%) and N_2 selectivity (91%), which was much superior to the A1-PdCu particles.[9] For electrochemical conversion of CO, the ordered PdCu electrocatalyst endowed a rather high CO-to-acetate selectivity at high current density, relative to the disordered PdCu one.[8] The high-density Cu−Pd pairs in the B2 catalyst enhanced *CO coverage, stabilized the ethenone intermediate, and thereby promoted acetate formation. The crystal phase of PdCu nanoparticles was also documented to affect the activity and selectivity in hydrogenation reactions of unsaturated compounds, where the ordered B2 particles showed superior performance compared to the disordered A1 ones.[10−17] For example, the B2-PdCu particles effectively catalyzed selective hydrogenation of 3-nitrostyrene with 94% selectivity for 3-nitro-ethylbenzene at 100% substrate conversion, but the A1-PdCu particles only showed 64% selectivity.[15] B2-PdCu nanocubes were highly selective and active for acetylene hydrogenation to ethylene, giving ethylene selectivity (95%) as compared to that on the A1-PdCu particles (68%).[16] The Pd single sites in the B2 catalyst adsorbed the intermediate $*C_2H_4$ via π-bonding, which facilitated the desorption of ethylene. Apparently, the crystal

phase of PdCu particles considerably affects their catalytic performance, primarily because of the electronic and geometric configurations of the surface metal atoms.

To date, PdCu nanoparticles are commonly prepared by liquid-phase approaches and typically adopt the disordered A1 structure that features a random mixing of Pd and Cu atoms. The crystal-phase transition from disordered A1 to ordered B2 is usually done at high temperatures and under inert/reducing atmospheres.[1,2,4,8−10,12,18−21] However, sintering of the PdCu particles and diffusion of Pd and Cu atoms between the particles under such harsh conditions result in a mixture of A1 and B2 particles with a dual-size distribution. The B2 particles have larger sizes, while the A1 particles are relatively smaller. Thus, it is difficult to elucidate the structure of the active sites over these bimetallic nanoparticles due to the interplay between particle size and crystal phase.

In a recent study, we have proposed a silica-confinement strategy to tune the crystal phase of PdCu at a single-nanoparticle scale.[22] Silica coating of monodisperse PdCu colloids yielded an unfirm core−shell geometry, where the silica shell spatially isolated each PdCu colloid and thus allowed crystal-phase transition between A1 and B2. As a consequence, the resulting B2 and A1 particles had the same size (around 8 nm) and chemical composition (Pd/Cu molar ratio of 1/1). When used to catalyze selective hydrogenation of acetylene to ethylene at room temperature, the B2 particles exhibited a much higher activity; the specific reaction rate was 1 order of magnitude greater than that of the A1 particle.[22] In this work, we extended the study to examine the crystal-phase-dependent behavior of these PdCu nanoparticles for catalytic reduction of NO by CO, a crucial reaction in the three-way catalysis for purifying vehicle exhaust emissions. It was found that the intrinsic activity of the B2 particles was 4.5 times greater than that of the A1 particle. The orderly arranged Pd and Cu atoms on the B2 particle surface favored the coadsorption of NO and CO and facilitated the dissociation of NO, thereby showing a much higher activity.

2. EXPERIMENTAL SECTION

2.1. Catalyst Preparation. Fabrication of PdCu colloids, silica coating the PdCu colloids, and crystal-phase transition of the PdCu nanoparticles have been described in our previous work.[22] The key procedures and synthetic conditions are introduced briefly as below.

2.1.1. PdCu Colloids. The PdCu colloids were prepared by reducing Pd^{2+} (sodium tetrachloropalladate) and Cu^{2+} (cupric chloride) with ethylene glycol. In a typical synthesis, 66.2 mg of Na_2PdCl_4 and 46.9 mg of $CuCl_2{\cdot}2H_2O$ were dissolved into 100 mL of ethylene glycol at room temperature under Ar flow, and 1 mL of oleylamine was added as the capping agent. The mixture was heated to 120 °C and kept at that temperature for 20 min under stirring; the mixture was further heated to 200 °C and maintained at that temperature for 2 h. After cooling down to room temperature, the solid product was collected by centrifugation, washed with cyclohexane and acetone mixture, and dispersed into cyclohexane (0.15 mg mL^{-1}).

2.1.2. Silica-Coated PdCu Colloids. Each PdCu colloid was then coated with a silica shell using a water-cyclohexane reverse microemulsion method at 20 °C. First, 80 mL of Triton X-100 (polyethylene glycol tert-octylphenyl ether) was added to 250 mL of PdCu colloid/cyclohexane solution (0.15 mg mL^{-1}). Then, aqueous ammonia solution (29.4 wt %, 5 mL) and aqueous hydrazine hydrate solution (80 wt %, 5 mL) were added to the mixture. Finally, 9.35 g tetraethyl orthosilicate, mixed with 250 mL cyclohexane, was added to the suspension and stirred for 1 h. The solid product was precipitated by adding 450 mL ethanol, collected by centrifugation, washed with ethanol, and dried at 50 °C for 12 h under vacuum, yielding silica-coated PdCu colloids.

2.1.3. B2/A1-PdCu Particles. The silica-coated PdCu colloids were then treated with H_2 at 400 °C for 2 h, yielding the B2 particle in the ordered body-centered cubic phase. The A1 particle in the disordered face-centered cubic phase was obtained by calcining the B2 particle at 400 °C in air for 4 h, followed by H_2 reduction at 500 °C for 2 h. Elemental analysis, using inductively coupled plasma atomic emission spectroscopy (ICPS-8100 Spectrometer), identified a Pd loading of 11.5 wt % and a Cu loading of 7.3 wt %, equaling a Pd/Cu molar ratio of 1/1.

2.2. Catalyst Characterizations. X-ray diffraction (XRD) patterns were recorded on a Rigaku D/MAX-2500/PC diffractometer using a Cu Kα radiation source that operated at 40 kV and 200 mA. In situ XRD measurements were done using a high-temperature chamber with the same instrument operated at 40 kV and 300 mA. 230 mg sample was pressed into a self-supporting wafer, mounted in the chamber, and heated from room temperature to 800 °C at a rate of 10 °C min^{-1} under the flow of a 5.0 vol % H_2/N_2 mixture (50 mL min^{-1}).

X-ray photoelectron spectroscopy (XPS) spectra were recorded over an ESCALAB 250Xi instrument (Thermofisher) using an Al Kα radiation source that operated at an accelerating voltage of 15 kV. The sample was pressed into a thin disc and mounted on a sample rod placed in the pretreatment chamber, where it was treated with a 5.0 vol % H_2/N_2 mixture (50 mL·min^{-1}) at 400 °C for 1 h and then purged by helium at 400 °C for 0.5 h. After cooling down to room temperature, the sample was transferred into the analysis chamber, where the spectra of Pd 3d, Cu 2p, and Cu L3VV were recorded. The charging effect was corrected by adjusting the binding energy of Si 2p to 104.4 eV.

Transmission electron microscopy (TEM) images were taken over a Hitachi 7700 microscope operated at 100 kV; high-resolution TEM (HRTEM) images were recorded on an FEI Tecnai G2 F30 S-Twin microscope operated at 300 kV. Aberration-corrected high-angle annular dark field scanning transmission electron microscopy (HAADF-STEM) images were acquired with a JEOL-ARM 300F microscope operated at 300 kV. Energy dispersive X-ray spectroscopy (EDS) elemental mappings over individual particles were collected using a JED-2300 T spectrometer. The specimen was prepared by ultrasonically dispersing the powder sample in ethanol, depositing droplets of the suspension onto lacey carbon-coated gold grids and drying in air.

Fourier transform IR spectroscopy (FTIR) of CO adsorption on the PdCu particles was conducted with a highly sensitive ultrahigh vacuum Fourier transform IR spectroscopy (UHV-FTIRS) system, dedicated to IR investigation on metal/oxide catalysts in the form of both macroscopic single crystals and powdered particles.[23,24] 200 mg portion of catalyst was pressed into an inert metal grid and mounted on a sample holder that was specially designed for the transmission model IR transmission measurements. The sample was pretreated with atomic hydrogen at 400 °C for 1 h and then exposed to CO at −163 °C and gradually heated to room temperature at a rate of 3 °C min^{-1}. IR data were accumulated by recording

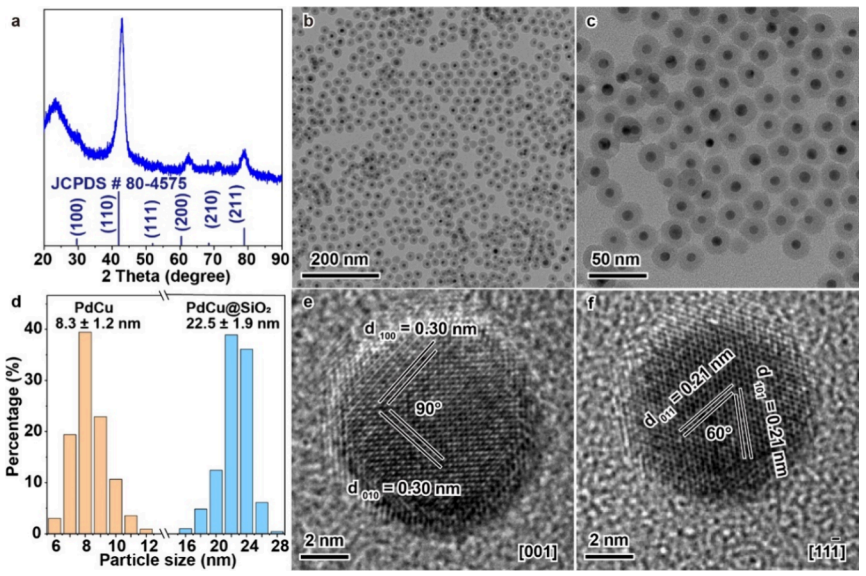

Figure 1. XRD pattern (a) and TEM images and size distribution (b–f) of the silica-coated PdCu colloids.

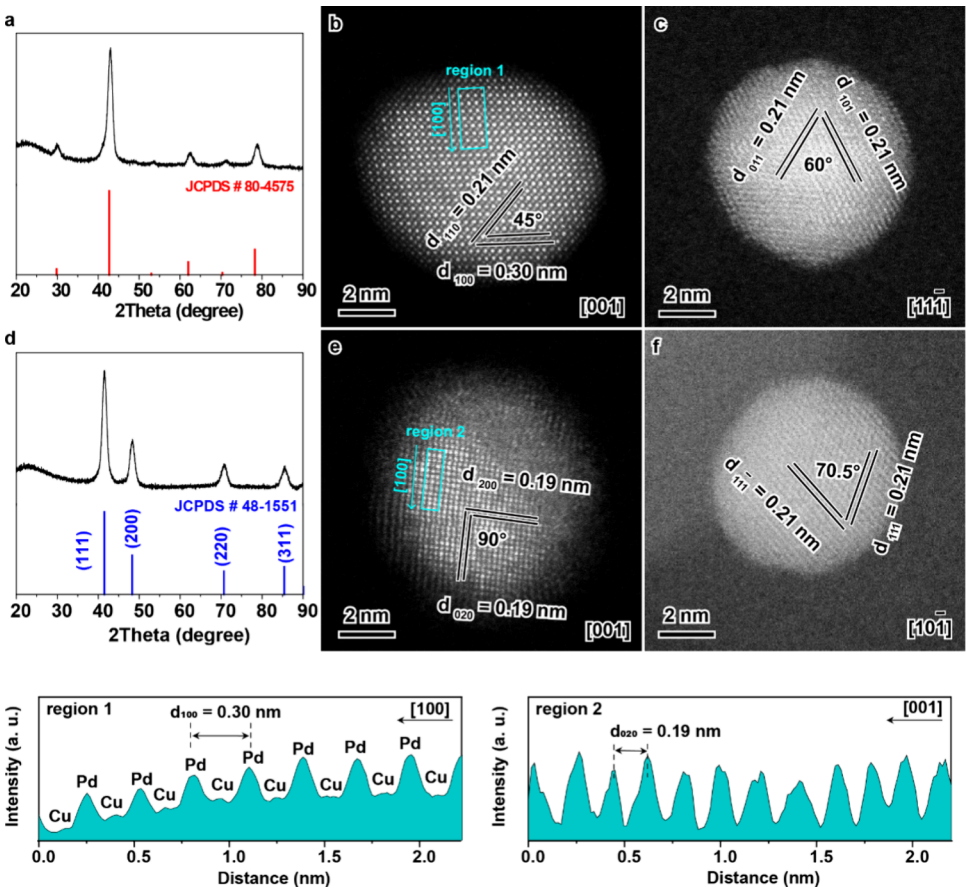

Figure 2. XRD patterns and TEM/STEM images of B2 (a–c) and A1 (d–f) particles.

1024 scans with a resolution of 4 cm^{-1} at the desired temperatures. Before each exposure, a spectrum of the clean sample was recorded as a background reference.

Temperature-programmed desorption (TPD) of NO or CO on the catalyst was conducted with a U-type quartz reactor. 150 mg sample (40–60 mesh) was pretreated with a 5.0 vol % H_2/Ar mixture (50 mL min^{-1}) at 400 °C for 1 h. After cooling down to room temperature under Ar flow (50 mL min^{-1}), the sample was exposed to a 1.0 vol % CO/He or 1.0 vol %NO/He mixture (50 mL min^{-1}) for 2 h and then purged by He for 1 h to remove the weakly adsorbed CO or NO. Subsequently, the sample was heated to 800 °C at a rate of 5 °C min^{-1} under He flow (50 mL min^{-1}), and the outlet gas was analyzed by an online mass spectrometer (Pfeiffer Omnistar).

2.3. Catalytic Test. NO by CO was conducted in a continuous-flow quartz tubular reactor. The catalyst (50 mg,

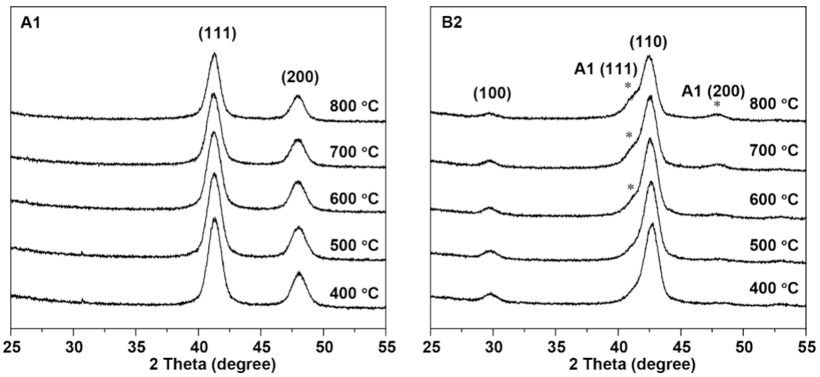

Figure 3. XRD patterns were recorded by heating the A1 and B2 particles from room temperature to 800 °C under hydrogen.

40−60 mesh) was pretreated with a 5.0 vol %H_2/He mixture (50 mL min^{-1}) at 400 °C for 1 h and then exposed to the reaction stream that contained 2000 ppm of NO and 2000 ppm of CO balanced with He (50 mL min^{-1}). The concentrations of nitrogen oxides and nitrogen in the inlet and outlet streams were monitored by a NO/NO_x analyzer (Thermo Environmental Instruments Inc.) and an online gas chromatograph (Agilent 7890B). The conversions of NO and CO were calculated according to the concentrations of NO and CO in the inlet and outlet gases, while the selectivity of N_2 was calculated based on the concentrations of N_2 and N_2O in the outlet gas.

$$\text{CO conversion} = ([CO]_{in} - [CO]_{out})/[CO]_{in} \times 100\%$$

$$\text{NO conversion} = ([NO]_{in} - [NO]_{out})/[NO]_{in} \times 100\%$$

$$N_2 \text{ selectivity} = [N_2]_{out}/([N_2]_{out} + [N_2O]_{out}) \times 100\%$$

For the kinetic study, the reaction rates were measured by controlling the conversion of NO below 20% via varying the flow rate of the reaction gas or the weight of the catalyst.

3. RESULTS AND DISCUSSION

3.1. Structures of the PdCu Particles. The spherical PdCu colloids had a mean size of 8.0 nm in the ordered B2 phase, as we described previously.[22] STEM analysis revealed that the PdCu colloid was enclosed by 12 {110} and 6 {100} facets; the {110} facet featured by the alternatively arranged Pd and Cu atoms, while the {100} facet was terminated by either Pd or Cu atoms (Figure S1). Each PdCu colloid was then coated with a silica shell, forming the core−shell geometry, where the metal core was sized at about 8.3 nm and the silica shell was 7.1 nm thick (Figure 1). The XRD pattern affirmed that the silica-coated PdCu colloids retained the ordered body-centered cubic phase (JCPDS # 80-4575). HRTEM images revealed the atomic structure of the silica-coated PdCu colloids. When viewed along the [001] direction, the vertical lattice spacings of 0.30 nm indicated the (100) and (100) planes. As viewed along the [11$\bar{1}$] direction, the two lattice spacings of 0.21 nm, with the dihedral angle of 60°, referred to the {011} planes.

H_2 treatment of the silica-coated PdCu colloids at 400 °C for 2 h eliminated the residual organic species (Figure S2), yielding the B2 particle (Figure 2a). TEM/STEM images confirmed that each PdCu particle was confined by a silica shell; the PdCu particle averaged at 8.5 nm, while the silica shell had a thickness of 7.4 nm (Figure S3). When viewed along the [001] zone axis, the lattice spacings of 0.30 and 0.21 nm with a dihedral angle of 45° referred to the (100) and (110) planes (Figure 2b). As viewed along the [11$\bar{1}$] direction, the two lattice spacings of 0.21 nm, at a dihedral angle of 60°, indicated the (011) and (101) planes (Figure 2c), respectively. When viewed along the [001] direction, the alternating bright and dim fringes indicated the well-organized Pd and Cu atomic columns (line intensity profile in region 1). Tuning of the crystal phase was done by treating the B2 particle with O_2 and H_2 at 400−500 °C. Air calcination of the B2 particle at 400 °C for 4 h and the subsequent H_2 reduction at 500 °C for 2 h yielded the A1 particle in the disordered fcc phase (Figure 2d). TEM analysis found that the PdCu particle was about 8.3 nm in size, while the silica shell had a thickness of approximately 7.1 nm (Figure S3). This evidenced that the silica shell prevented the PdCu particles from sintering during the high-temperature treatments by the reactive gases. STEM images detailed the atomic arrangement in the A1 particle. As projected along the [001] direction, the two orthogonal lattice spacings of 0.19 nm were assigned for the (200) and (002) planes (Figure 2e). The interplanar spacings of 0.21 nm with dihedral angle of 70.5° referred to the (111) and (1$\bar{1}$1) planes (Figure 2f). Line intensity profile of marked region 2 showed a consistent contrast, indicating the random distribution of Pd and Cu atoms. Accordingly, the A1 particle was projected to be enclosed by the {111} and {100} facets with random arrangements of Pd and Cu atoms.

These XRD and TEM/STEM data collectively attested that the crystal-phase transition from the ordered B2 phase to the disordered A1 structure occurred on the single-nanoparticle scale. Therefore, the B2 and A1 particles had approximately the same size and chemical composition but completely different crystal phases. Of note, this silica-coated crystal-phase transition differs from conventional cases where the PdCu particles are dispersed over oxide supports. When heated to high temperatures, crystal-phase transition and particle sintering take place simultaneously. The resulting PdCu particles possess a mixed phase: smaller particles in the A1 phase, while large ones in the B2 phase.[25] Here, the silica shell, acting as a diffusion barrier, eliminated participle sintering and allowed only intraparticle rearrangement of metal atoms during the crystal-phase transition. In situ XRD patterns, recorded by heating the samples from room temperature to 800 °C under the flow of a 5.0 vol % H_2/N_2 mixture, revealed the thermal stabilities of the A1 and B2 particles (Figure 3). The A1 particle kept the fcc phase in the entire temperature range without obvious changes in the diffraction lines. The B2 particle retained the ordered phase below 500 °C, while minor

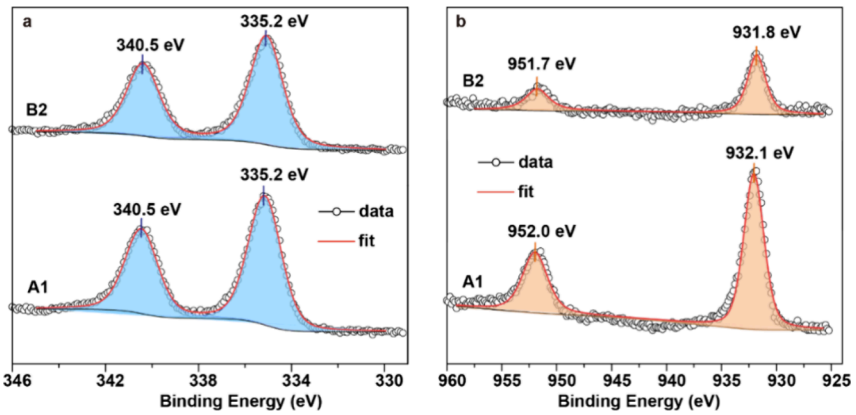

Figure 4. XPS spectra of Pd 3d (a) and Cu 2p (b) in particles B2 and A1 particles.

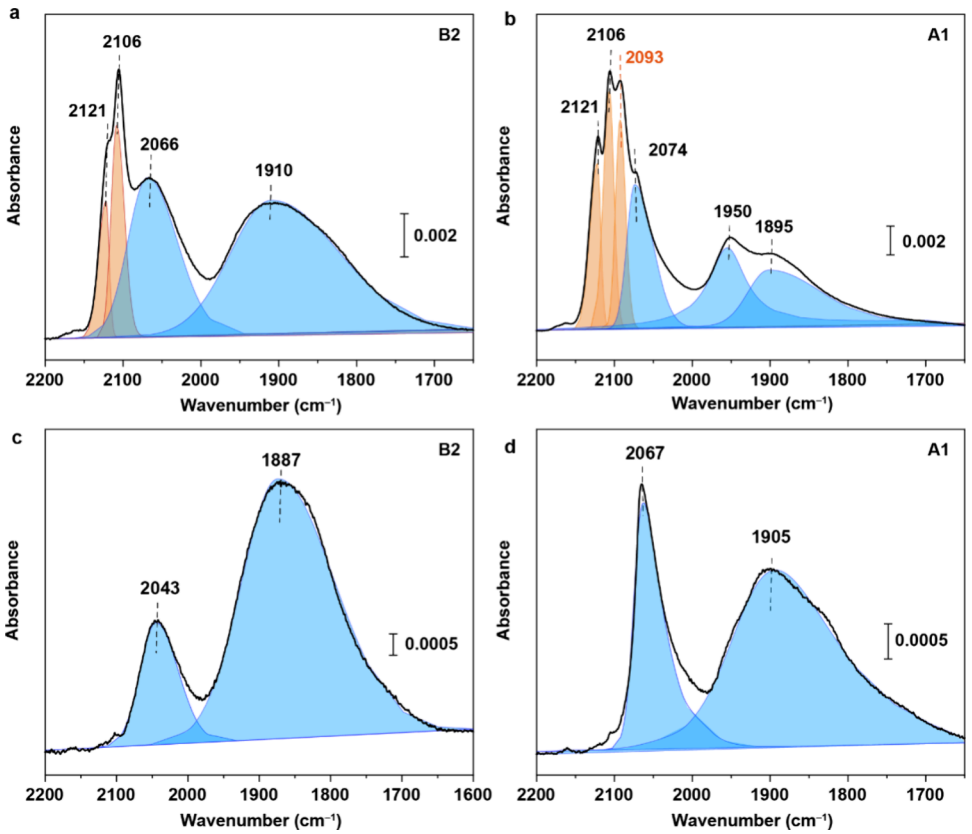

Figure 5. CO-IR spectra of the B2 and A1 particles recorded at −93 °C (a,b) and 27 °C (c,d).

A1 phase appeared at above 600 °C. The diffraction line corresponding to the (111) plane of the A1 phase emerged at 600 °C, while the diffraction line of the (200) plane became appreciable at 800 °C. This meant that the B2 particle experienced crystal-phase transition from B2 to A1 at above 600 °C. Nevertheless, the ordered body-centered cubic structure still dominated even at 800 °C.

3.2. Surface Properties of the PdCu Particles. XPS spectra identified the chemical states of Pd and Cu in particles B2 and A1 (Figure 4). In the Pd 3d spectra, the binding energies of $3d_{5/2}$ and $3d_{3/2}$ were located at 335.2 and 340.5 eV in both cases, which could be ascribed to metallic Pd in general. However, they were higher by 0.3 eV as compared with the values for monometallic Pd^0 (334.9 and 340.2 eV),[26,27] primarily because of the charge transfer in PdCu nanoparticles.[26,28,29] XPS spectra for Cu 2p, featured by spin−orbit splitting (Cu $2p_{3/2}$ and Cu $2p_{1/2}$), showed doublets at 932.1 and 952.0 eV for the A1 particle and at 931.8 and 951.7 eV for the B2 particle. They could be ascribed to metallic Cu, as further supported by the absence of satellites and the corresponding Cu L3VV spectra (Figure S4). These binding energies for Cu were much lower than these of monometallic Cu^0 (933.0 and 952.8 eV).[30,31] This is due to the electronic interaction in PdCu nanoparticles, where Pd transfers electrons to Cu through forming Pd−Cu bonds between the almost full "sd" levels of Pd and the resonant "dsp" levels of Cu near their Fermi levels.[28,29,32] The empty conduction band levels of Cu become partially occupied upon alloying with Pd, which readjusts the electronic structure of Cu and thus affects the binding energy of the core level. However, the electronic

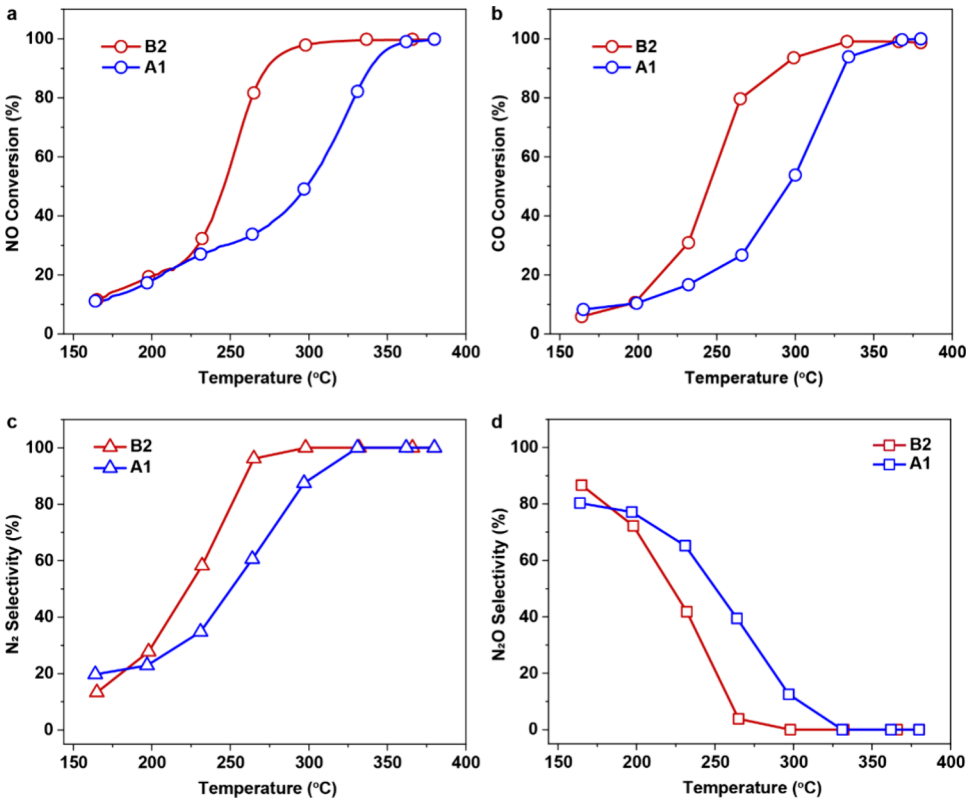

Figure 6. NO reduction by CO over the B2 and A1 particles. (a) NO conversion, (b) CO conversion, (c) N_2 selectivity, and (d) N_2O selectivity.

structure of Pd is less affected by this interaction because of the occupied states of Pd in the Pd−Cu bonds. Of note, the binding energies of Cu 2p in the B2 particle were lower by 0.3 eV than those for the A1 particle, implicating a stronger electronic interaction between Pd and Cu in the B2 phase.

CO-IR spectra elucidated the geometric and electronic properties of surface Pd and Cu atoms over the PdCu particles. Upon CO adsorption on the B2 particle at −93 °C, four distinct bands appeared at 2121, 2106, 2066, and 1910 cm^{-1} (Figure 5a). The broad band at 1910 cm^{-1} was attributed to CO bound to the bridged and hollow sites on contiguous Pd ensembles, while the band at 2066 cm^{-1} referred to CO linearly adsorbed on the isolated Pd site that coordinated to Cu atoms.[22,33−36] The band at 2121 cm^{-1} was assigned to CO adsorbed on isolated Cu site surrounded by Pd atoms, while the signal at 2106 cm^{-1} was ascribed to CO bound at Cu contiguous monolayers.[22,33,35−37] Over the A1 particle, an additional band appeared at 2093 cm^{-1} (Figure 5b), indicating CO bound to Cu multilayered aggregates.[22,38] The band for CO adsorbed on the isolated Pd site was resolved at 2074 cm^{-1}, which red-shifted by 8 cm^{-1} relative to that on the B2 particle (2066 cm^{-1}). For the CO-IR spectra, recorded at room temperature, only weak bands for CO bound to Pd-related sites were detected, while the Cu-related signals disappeared (Figure 5c,d). This indicated weaker adsorption of CO on Cu sites due to the $\sigma-\sigma$ repulsion between the half-filled Cu 4s orbital and the CO 5σ lone pair. On the B2 particle, linearly and bridge-bonded CO on Pd sites red-shifted to 2043 and 1887 cm^{-1}, respectively. On the A1 particle, the band for linear CO-Pd located at 2067 cm^{-1}, while that for bridge CO-Pd emerged at 1905 cm^{-1}. The discrepancy of vibration frequencies implied that CO bonded more strongly on the B2 particle, which involved back-donation from Pd 4d to CO 2π* orbitals.[34]

3.3. NO Reduction by CO over the PdCu Particles. Catalytic reduction of NO by CO is a key reaction in three-way catalysis for abating exhaust gases from vehicle emissions. Over Pd catalysts, this reaction follows the Langmuir−Hinshelwood mechanism.[39−41] NO and CO adsorb competitively on the Pd surface, and the adsorbed NO further dissociates into reactive N and O species; the N atoms combine to N_2, while the O atoms react with CO to yield CO_2.[42−44] Meanwhile, the activated N species, adsorbed strongly on the Pd surface, could interact with NO to form N_2O, desorbed as the byproduct.[45] However, the Pd surface favors a preferential adsorption of CO in the presence of NO, and the preadsorbed NO could be replaced by CO.[43] Alloying Pd with Cu has been documented to promote the activity/selectivity via the ligand and geometric effects.[46−53] For example, PdCu particles supported on CeO_2/Al_2O_3 catalyzed NO reduction by CO efficiently, giving a 100% conversion of NO at around 350 °C.[47] It was proposed that Cu in the PdCu particles modified the Pd valence state and activated the N−O bond. More recently, Pd_1Cu_5 single-atom alloys displayed a complete conversion of NO to N_2 even at 175 °C, where NO dissociation on Cu was proposed to be the rate-determining step.[50]

The B2 and A1 particles were tested for NO reduction by CO, where a prominent crystal-phase-dependent effect was observed (Figure 6). On the B2 particle, NO conversion was 20% at 200 °C, increased sharply with raising the temperature, and approached nearly 100% at 275 °C. For the A1 particle, NO conversion was 20% at 200 °C as well, but it increased to 32% at 250 °C and then reached about 100% at 325 °C. These results evidenced that the B2 particle was more active than the A1 particle. The selectivity toward N_2 depended on the

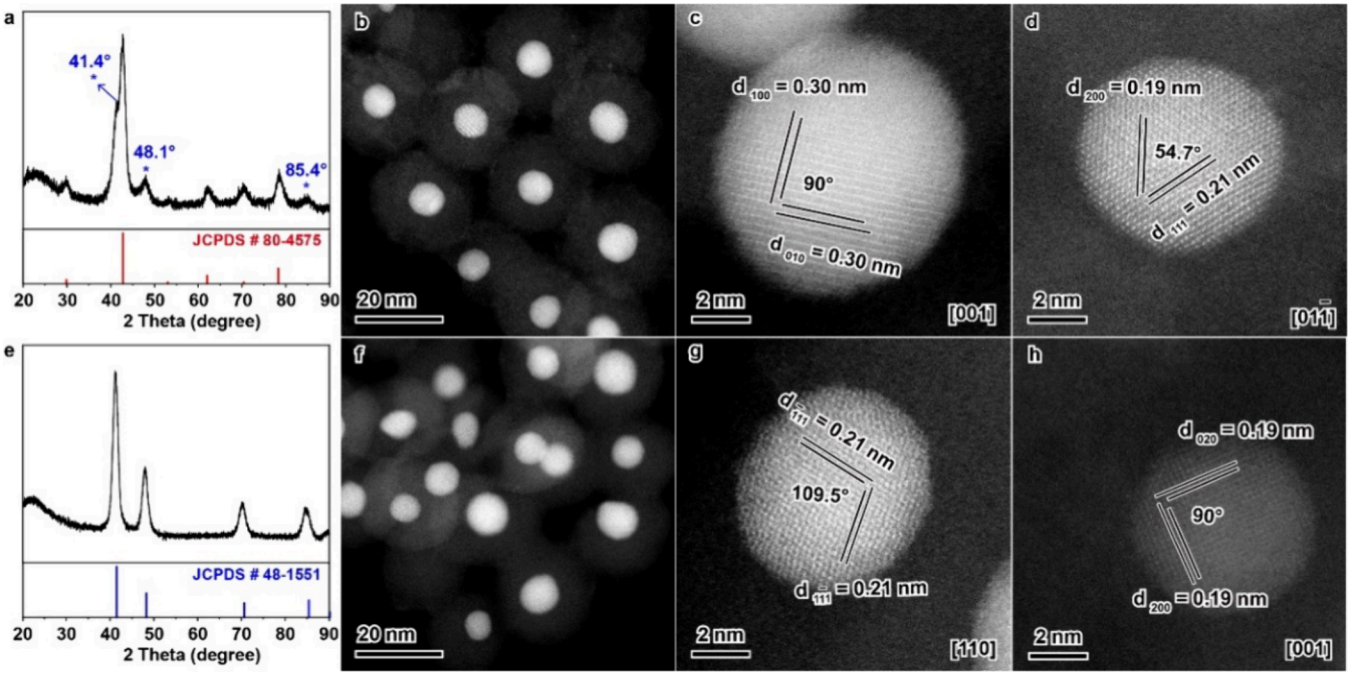

Figure 7. XRD patterns and STEM images of the used B2 (a–d) and A1 particles (e–h).

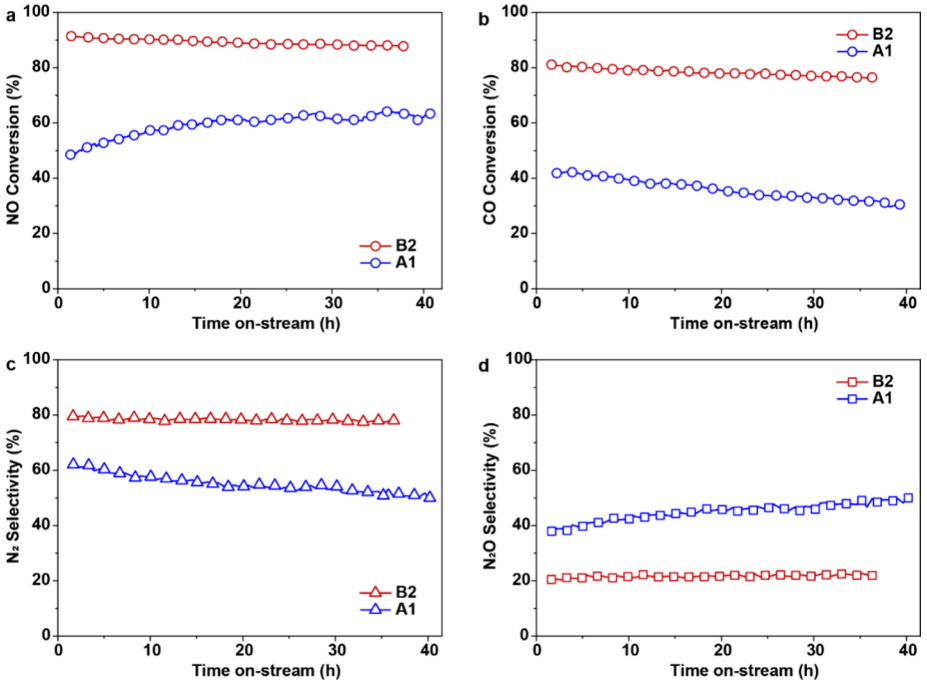

Figure 8. NO reduction by CO over the B2 and A1 particles at 260 °C. (a) NO conversion, (b) CO conversion, (c) N_2 selectivity, and (d) N_2O selectivity.

reaction temperature over both catalysts. N_2O was the predominant product at low temperatures, while N_2 became the main product at higher temperatures. In line with the full conversion of NO, nearly 100% selectivity toward N_2 was achieved at 275 °C on the B2 particle and at 325 °C on the A1 particle. Here, the silica shells in the B2 and A1 particles did not affect the catalytic performances. The surface area was 177 $m^2\ g^{-1}$ for the B2 particle while 161 $m^2\ g^{-1}$ for the A1 particle. Both samples had a similar pore size of 0.52–0.53 nm on the silica shells (Figure S5). This allowed diffusion of the reacting molecules, e.g., NO (0.349 nm), CO (0.369 nm), CO_2 (0.33 nm), N_2O (0.383 nm), and N_2 (0.380 nm),[54] to the core bimetallic particles for their chemical transformations.

XRD and STEM analyses on the used PdCu catalysts in Figure 6 revealed structural changes under the reaction conditions. The used B2 particle dominated in the ordered body-centered cubic phase, but minor A1 phase appeared as evidenced by the additional diffraction lines at 2theta of 41.4, 48.1, and 85.4° (Figure 7a). This meant that the B2 particle crystallized into mixed B2 and A1 phases during NO reduction

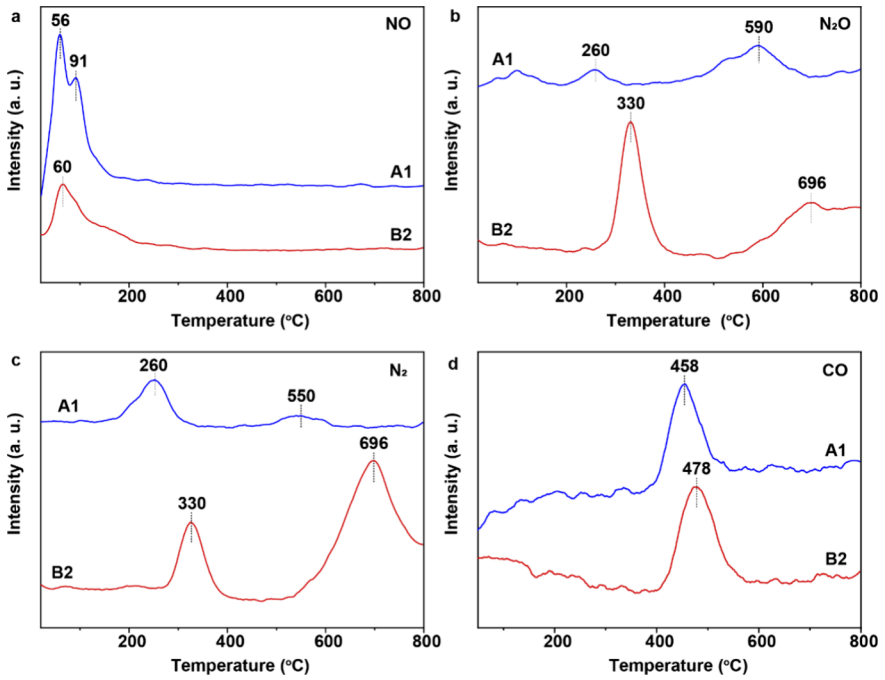

Figure 9. TPD profiles of NO and CO over the B2 and A1 particles. (a–c) NO, N_2O, and N_2 desertions and (d) CO desorption.

by CO. It is highly likely that this crystal-phase transition was driven by the adsorbed oxygen species generated by NO dissociation. STEM images verified the core–shell geometry, where the core metal particle (8.2 nm) was confined by the silica shell with a thickness of 7.0 nm (Figures 7b and S6). The two-perpendicular lattice spacings of 0.30 nm, viewed along the [001] direction, indexed the {010} facets (Figure 7c). However, the two lattice spacings of 0.21 and 0.19 nm, with dihedral angle of 54.7°, indicated the (111) and (200) planes of the A1 phase (Figure 7d), respectively. The used A1 particle retained the disordered face-centered cubic phase (Figure 7e), which was further supported by the STEM images (Figure 7f–h). As viewed along the [110] direction, the lattice spacings of 0.21 nm with a dihedral angle of 109.5° referred to the {111} facets, while the orthogonal lattice spacings of 0.19 nm indicated the (200) and (020) planes of the A1 phase, when viewed along the [001] direction. The metal size and the silica shell thickness remained the same as in the fresh catalyst (Figure S6).

To avoid crystal-phase transition during the reaction, the B2 and A1 particles were then tested for NO reduction by CO at 260 °C (Figure 8). The B2 particle showed stable performance of 90% NO conversion and 80% N_2 selectivity for 38 h. On the A1 particle, the conversion of NO was 48% at the initial stage but gradually increased to 62% at 40 h, while the corresponding selectivity of N_2 declined from 68 to 50%. The reaction rates, measured by controlling the conversion of NO below 20% at 260 °C (Figure S7), further demonstrated the superior activity of the B2 particle. The conversion rate of NO on the B2 particle was 3.6×10^{-6} mol_{NO} g_{cat}^{-1} s^{-1}, which was 4.5 times of that (8.0×10^{-7} mol_{NO} g_{cat}^{-1} s^{-1}) on the A1 particle. XRD patterns of the used samples in Figure 8 verified the well retained B2 and A1 phases in the respective catalysts (Figure S8). XPS spectra of the used samples revealed that Pd and Cu were oxidized slightly after the reaction tests (Figure S9). The binding energies of Pd 3d were located at 335.2 and 340.5 eV in both catalysts, which are generally ascribed to metallic Pd. While the binding energies at 367.9 and 342.2 eV indicated Pd^{2+}, the binding energies of Cu 2p at 932.6/952.5 eV for the used A1 particle and those at 932.3/952.2 eV for the B2 particle were assigned to metallic Cu. However, the satellites at 940–950 eV evidenced the partial oxidation of Cu during the reactions.

All of these reaction data demonstrated that the crystal phase of PdCu particles affected the performance for NO reduction by CO, in which the B2 phase outperformed the A1 phase. NO-TPD experiments elucidated the adsorption behavior of NO on particles B2 and A1 (Figure 9). NO and N_2O/N_2 desorbed from the catalysts as the temperature rises. Over the B2 particle, minor desorption of NO occurred at 60 °C, while intense desorptions of N_2O/N_2 appeared at 330 and 696 °C, suggesting that the preadsorbed NO dissociated on the metal surface and desorbed as N_2O/N_2.[53,55–58] Most likely, NO dissociated into reactive N and O species, and the N atoms combined to N_2 or interacted with another NO to form N_2O.[45] On the A1 particle, intense desorptions of NO at 56/91 °C and minor desorptions of N_2O/N_2 at 260/590 °C were detected. Therefore, it is reasonable to infer that NO was mainly molecularly adsorbed on the A1 catalyst while mostly dissociatively adsorbed on the B2 catalyst. CO-TPD profiles of the A1 and B2 catalysts showed practically identical CO desorptions at 458–478 °C, corresponding to the molecularly adsorbed CO.[59,60]

As mentioned above, the catalytic reduction of NO by CO follows the Langmuir–Hinshelwood mechanism, during which NO and CO adsorb competitively on the catalyst surface. Over PdCu particles, NO interacts more favorably with the Cu atoms due to the higher oxophilicity, while CO adsorbs preferentially on the Pd atoms because of the stronger d-π back-donation.[50,53,57,61–64] At this scenario, Cu atoms are responsible for the dissociative adsorption of NO, while Pd atoms serve as the sites for the molecular adsorption of CO. First, NO adsorbs on the Cu atoms and dissociates into reactive N and O species. Then, the activated N atoms

combine to N_2 and/or reacts with another NO to form N_2O, depending on the temperature. Finally, the released O species reacts with adsorbed CO on the neighboring Pd atoms to yield CO_2. Here, the B2 particle was mainly enclosed by the {110} facets, over which the alternatively arranged Pd and Cu atoms favored the coadsorption of CO and NO. This process could be kinetically facilitated by the neighboring Pd and Cu atoms, involving charge transfer.[47,50,62] By contrast, the A1 particle predominantly exposed the {111} facets, where the Cu and Pd atoms were distributed randomly. The competitive adsorption of NO and CO over the A1 particle surface resulted in lower activity.

4. CONCLUSIONS

The crystal phase of the PdCu nanoparticle was mediated between the ordered body-centered cubic and disordered face-centered cubic phases. The porous silica shell effectively prevented the bimetallic particle from sintering at high temperatures and under reactive gases during the crystal-phase transition. The resulting PdCu particles had approximately the same size and chemical composition but totally differed c rystal p hase. T he B 2 p article w as predominantly enclosed by the {110} facets, where isolated Pd and Cu atoms were arranged orderly, while the A1 particle primarily exposed the {111} facets terminated by a random distribution of Pd and Cu atoms. These PdCu particles showed remarkable crystal-phase-dependent behavior in the catalytic reduction of NO by CO. The reaction rate over the B2 particle was 4.5 times greater than that of the A1 particle. This was ascribed to the alternating arrangement of Pd and Cu atoms on the {110} facets exposed by the B2 particle, which favored the coadsorption of NO and CO and more importantly facilitated the dissociation of NO.

AUTHOR INFORMATION

Corresponding Author

Wenjie Shen − *State Key Laboratory of Catalysis, Dalian Institute of Chemical Physics, Chinese Academy of Sciences, Dalian 116023, China;* orcid.org/0000-0002-3071-9556; Email: shen98@dicp.ac.cn

Authors

Shuang Liu − *State Key Laboratory of Catalysis, Dalian Institute of Chemical Physics, Chinese Academy of Sciences, Dalian 116023, China;* orcid.org/0000-0002-0916-1834

Yong Li − *State Key Laboratory of Catalysis, Dalian Institute of Chemical Physics, Chinese Academy of Sciences, Dalian 116023, China;* orcid.org/0000-0003-4830-9210

Yuemin Wang − *Institute of Functional Interfaces, Karlsruhe Institute of Technology, Eggenstein-Leopoldshafen 76344, Germany;* orcid.org/0000-0002-9963-5473

Author Contributions

S.L.: methodology, formal analysis, investigation, writing−original draft, visualization and funding acquisition. Y.L.: investigation, formal analysis, writing−reviewing and editing. Y.W.: investigation and formal analysis. W.S.: conceptualization, investigation, formal analysis, writing−reviewing and editing.

Notes

The authors declare no competing financial interest.

ACKNOWLEDGMENTS

This work was financially supported by the National Key Research & Development Program of China (2023YFA1508500). Y.W. thanks the support by the Deutsche Forschungsgemeinschaft (DFG, German Research Foundation) − Project-ID 426888090-SFB 1441.

REFERENCES

(1) Ma, S.; Sadakiyo, M.; Heima, M.; Luo, R.; Haasch, R. T.; Gold, J. I.; Yamauchi, M.; Kenis, P. J. A. Electroreduction of carbon dioxide to hydrocarbons using bimetallic Cu−Pd catalysts with different mixing patterns. *J. Am. Chem. Soc.* **2017**, *139*, 47−50.

(2) Qiu, Y.; Xin, L.; Li, Y.; McCrum, I. T.; Guo, F.; Ma, T.; Ren, Y.; Liu, Q.; Zhou, L.; Gu, S.; et al. BCC-phased PdCu alloy as a highly active electrocatalyst for hydrogen oxidation in alkaline electrolytes. *J. Am. Chem. Soc.* **2018**, *140*, 16580−16588.

(3) Jiang, X.; Nie, X.; Wang, X.; Wang, H.; Koizumi, N.; Chen, Y.; Guo, X.; Song, C. Origin of Pd-Cu bimetallic effect for synergetic promotion of methanol formation from CO_2 hydrogenation. *J. Catal.* **2019**, *369*, 21−32.

(4) Tong, W.; Huang, B.; Wang, P.; Li, L.; Shao, Q.; Huang, X. Crystal-phase-engineered PdCu electrocatalyst for enhanced ammonia synthesis. *Angew. Chem., Int. Ed.* **2020**, *59*, 2649−2653.

(5) Zhang, G.; Shi, Y.; Fang, Y.; Cao, D.; Guo, S.; Wang, Q.; Chen, Y.; Cui, P.; Cheng, S. Ordered PdCu-based core−shell concave nanocubes enclosed by high-index facets for ethanol electrooxidation. *ACS Appl. Mater. Interfaces* **2021**, *13*, 33147−33156.

(6) Gao, Q.; Pillai, H. S.; Huang, Y.; Liu, S.; Mu, Q.; Han, X.; Yan, Z.; Zhou, H.; He, Q.; Xin, H.; et al. Breaking adsorption-energy scaling limitations of electrocatalytic nitrate reduction on intermetallic CuPd nanocubes by machine-learned insights. *Nat. Commun.* **2022**, *13*, 2338.

(7) Li, X.; Liu, Y.; Zhang, J.-J.; Yan, B.; Jin, C.; Dou, J.; Li, M.; Feng, X.; Liu, G. No annealing synthesis of ordered intermetallic PdCu nanocatalysts for boosting formic acid oxidation. *Chem. Mater.* **2022**, *34*, 1385−1391.

(8) Ji, Y.; Chen, Z.; Wei, R.; Yang, C.; Wang, Y.; Xu, J.; Zhang, H.; Guan, A.; Chen, J.; Sham, T.-K.; et al. Selective CO-to-acetate electroreduction via intermediate adsorption tuning on ordered Cu−Pd sites. *Nat. Catal.* **2022**, *5*, 251−258.

(9) Lim, J.; Cullen, D. A.; Stavitski, E.; Lee, S. W.; Hatzell, M. C. Atomically ordered PdCu electrocatalysts for selective and stable electrochemical nitrate reduction. *ACS Energy Lett.* **2023**, *8*, 4746−4752.

(10) Friedrich, M.; Villaseca, S. A.; Szentmiklosi, L.; Teschner, D.; Armbrüester, M. Order-induced selectivity increase of $Cu_{60}Pd_{40}$ in the semi-hydrogenation of acetylene. *Materials* **2013**, *6*, 2958−2977.

(11) Zhang, L.; Zhou, M.; Wang, A.; Zhang, T. Selective hydrogenation over supported metal catalysts: from nanoparticles to single atoms. *Chem. Rev.* **2020**, *120*, 683−733.

(12) Yang, T.; Feng, Y.; Ma, R.; Li, Q.; an, H.; Liu, Y.; He, Y.; Miller, J. T.; Li, D. Improvement of selectivity in acetylene hydrogenation with comparable activity over ordered PdCu catalysts induced by post-treatment. *ACS Appl. Mater. Interfaces* **2021**, *13*, 706−716.

(13) Dasgupta, A.; He, H.; Gong, R.; Shang, S.-L.; Zimmerer, E. K.; Meyer, R. J.; Liu, Z.-K.; Janik, M. J.; Rioux, R. M. Atomic control of active-site ensembles in ordered alloys to enhance hydrogenation selectivity. *Nat. Chem.* **2022**, *14*, 523−529.
(14) Guo, M.; Ma, P.; Wei, L.; Wang, J.; Wang, Z.; Zheng, K.; Cheng, D.; Liu, Y.; Dai, H.; Guo, G.; et al. Highly selective activation of C−H bond and inhibition of C−C bond cleavage by tuning strong oxidative Pd sites. *J. Am. Chem. Soc.* **2023**, *145*, 11110−11120.
(15) Li, P.; Liu, X.; Guo, M.; Pi, Y.; Wang, N.; Bai, S.; Xu, Y.; Sun, Q. Stable and ordered body-centered cubic PdCu phase for highly selective hydrogenation. *Small Methods* **2023**, *7*, No. e2201356.
(16) Gao, Q.; Yan, Z.; Zhang, W.; Pillai, H. S.; Yao, B.; Zang, W.; Liu, Y.; Han, X.; Min, B.; Zhou, H.; et al. Atomic layers of B2 CuPd on Cu nanocubes as catalysts for selective hydrogenation. *J. Am. Chem. Soc.* **2023**, *145*, 19961−19968.
(17) Zhai, P.; Cullen, D. A.; Ding, K. The role of surface chemistry in the synthesis of supported CuPd bimetallic/intermetallic catalysts for selective hydrogenation reactions. *Chem. Eng. J.* **2024**, *480*, No. 148238.
(18) Yamauchi, M.; Tsukuda, T. Production of an ordered (B2) CuPd nanoalloy by low-temperature annealing under hydrogen atmosphere. *Dalton Trans.* **2011**, *40*, 4842−4845.
(19) Fan, Z.; Zhang, H. Crystal phase-controlled synthesis, properties and applications of noble metal nanomaterials. *Chem. Soc. Rev.* **2016**, *45*, 63−82.
(20) Chen, Y.; Lai, Z.; Zhang, X.; Fan, Z.; He, Q.; Tan, C.; Zhang, H. Phase engineering of nanomaterials. *Nat. Rev. Chem.* **2020**, *4*, 243−256.
(21) Zhao, J.-W.; Wang, H.-Y.; Feng, L.; Zhu, J.-Z.; Liu, J.-X.; Li, W.-X. Crystal-phase engineering in heterogeneous catalysis. *Chem. Rev.* **2024**, *124*, 164−209.
(22) Liu, S.; Li, Y.; Yu, X.; Han, S.; Zhou, Y.; Yang, Y.; Zhang, H.; Jiang, Z.; Zhu, C.; Li, W.; et al. Tuning crystal-phase of bimetallic singlenanoparticle for catalytic hydrogenation. *Nat. Commun.* **2022**, *13*, 4559.
(23) Wang, Y.; Wöll, C. IR spectroscopic investigations of chemical and photochemical reactions on metal oxides: bridging the materials gap. *Chem. Soc. Rev.* **2017**, *46*, 1875−1932.
(24) Wang, Y.; Glenz, A.; Muhler, M.; Wöll, C. A new dual-purpose ultrahigh vacuum infrared spectroscopy apparatus optimized for grazing-incidence reflection as well as for tansmission geometries. *Rev. Sci. Instrum.* **2009**, *80*, 113108.
(25) Friedrich, M.; Armbrüster, M. Crystallite size controls the crystal structure of $Cu_{60}Pd_{40}$ nanoparticles. *Chem. Mater.* **2009**, *21*, 5886−5891.
(26) Marakatti, V. S.; Sarma, S. C.; Joseph, B.; Banerjee, D.; Peter, S. C. Synthetically tuned atomic ordering in PdCu nanoparticles with nnhanced catalytic activity toward solvent-free benzylamine oxidation. *ACS Appl. Mater. Interfaces* **2017**, *9*, 3602−3615.
(27) Boucher, M. B.; Zugic, B.; Cladaras, G.; Kammert, J.; Marcinkowski, M. D.; Lawton, T. J.; Sykes, E. C. H.; Flytzani-Stephanopoulos, M. Single atom alloy surface analogs in $Pd_{0.18}Cu_{15}$ nanoparticles for selective hydrogenation reactions. *Phys. Chem. Chem. Phys.* **2013**, *15*, 12187−12196.
(28) Rochefort, A.; Abon, M.; Delichere, P.; Bertolini, J. C. Alloying effect on the adsorption properties of $Pd_{50}Cu_{50}\{111\}$ single crystal surface. *Surf. Sci.* **1993**, *294*, 43−52.
(29) Cho, E.-J.; Lee, S.; Oh, S. J.; Han, M.; Lee, Y. S.; Whang, C. N. Unoccupied states and charge transfer in Cu-Pd alloys studied by bremsstrahlung isochromat spectroscopy, X-ray photoelectron spectroscopy, and LIII absorption spectroscopy. *Phys. Rev. B* **1995**, *52*, 16443−16450.
(30) Zong, Z.; Tan, H.; Zhang, P.; Yuan, C.; Zhao, R.; Song, F.; Yi, W.; Zhang, F.; Cui, H. Cu/SiO_2 synthesized with HKUST-1 as precursor: high ratio of $Cu^+/(Cu^+ + Cu^0)$ and rich oxygen defects for efficient catalytic hydrogenation of furfural to 2-methyl furan. *Phys. Chem. Chem. Phys.* **2023**, *25*, 24377−24385.
(31) Hai, Y.; Guan, T.; Feng, Y.; Zhen, Z.; Yang, Y.; Hu, Y.; Lv, J.; Wang, Y.; Ma, X. Facile synthesis of $Cu@Ag/SiO_2$ catalysts for the selective hydrogenation of dimethyl oxalate to methyl glycolate. *Chem. Eng. Sci.* **2024**, *294*, No. 120121.
(32) Efremenko, I.; Sheintuch, M. DFT study of small bimetallic palladium−copper clusters. *Chem. Phys. Lett.* **2005**, *401*, 232−240.
(33) Kruppe, C. M.; Krooswyk, J. D.; Trenary, M. Polarization-dependent infrared spectroscopy of adsorbed carbon monoxide to probe the surface of a Pd/Cu(111) single-atom alloy. *J. Phys. Chem. C* **2017**, *121*, 9361−9369.
(34) Lear, T.; Marshall, R.; Lopez-Sanchez, J. A.; Jackson, S. D.; Klapötke, T. M.; Bäumer, M.; Rupprechter, G.; Freund, H. J.; Lennon, D. The application of infrared spectroscopy to probe the surface morphology of alumina-supported palladium catalysts. *J. Chem. Phys.* **2005**, *123*, 174706.
(35) Rupprechter, G. Sum frequency generation and polarization−modulation infrared reflection absorption spectroscopy of functioning model catalysts from ultrahigh vacuum to ambient pressure. *Adv. Catal.* **2007**, *51*, 133−263.
(36) McCue, A. J.; Anderson, J. A. CO induced surface segregation as a means of improving surface composition and enhancing performance of CuPd bimetallic catalysts. *J. Catal.* **2015**, *329*, 538−546.
(37) Ball, M. R.; Rivera-Dones, K. R.; Gilcher, E. B.; Ausman, S. F.; Hullfish, C. W.; Lebrón, E. A.; Dumesic, J. A. AgPd and CuPd catalysts for selective hydrogenation of acetylene. *ACS Catal.* **2020**, *10*, 8567−8581.
(38) Hoffmann, F. M.; Paul, J. A FT-IRAS study of the vibrational properties of CO adsorbed on Cu/Ru(001). *II. the dispersion of copper. J. Chem. Phys.* **1987**, *87*, 1857−1865.
(39) Wang, J.; Chen, H.; Hu, Z.; Yao, M.; Li, Y. A review on the Pd-based three-way catalyst. *Catal. Rev.* **2015**, *57*, 79−144.
(40) Gholami, Z.; Luo, G.; Gholami, F.; Yang, F. Recent advances in selective catalytic reduction of NO_x by carbon monoxide for flue gas cleaning process: a review. *Catal. Rev.-Sci. Eng.* **2021**, *63*, 68−119.
(41) Wang, Y. X.; Xu, W. Q.; Liu, H. X.; Chen, W. R.; Zhu, T. Y. Catalytic removal of gaseous pollutant NO using CO: Catalyst structure and reaction mechanism. *Environ. Res.* **2024**, *246*, No. 118037.
(42) Holles, J. H.; Switzer, M. A.; Davis, R. J. Influence of ceria and lanthana promoters on the kinetics of NO and N_2O Reduction by CO over alumina-supported palladium and rhodium. *J. Catal.* **2000**, *190*, 247−260.
(43) Mamede, A. S.; Leclercq, G.; Payen, E.; Granger, P.; Grimblot, J. In situ Raman characterisation of surface modifications during NO transformation over automotive Pd-based exhaust catalysts. *J. Mol. Struct.* **2003**, *651*, 353−364.
(44) Granger, P.; Dhainaut, F.; Pietrzik, S.; Malfoy, P.; Mamede, A. S.; Leclercq, L.; Leclercq, G. An overview: Comparative kinetic behaviour of Pt, Rh and Pd in the NO + CO and NO + H_2 reactions. *Top. Catal.* **2006**, *39*, 65−76.
(45) Granger, P.; Dujardin, C.; Paul, J. F.; Leclercq, G. An overview of kinetic and spectroscopic investigations on three-way catalysts: mechanistic aspects of the CO + NO and CO + N_2O reactions. *J. Mol. Catal. A: Chem.* **2005**, *228*, 241−253.
(46) Kerkar, R. D.; Salker, A. V. Synergistic effect of modified Pd-based cobalt chromite and manganese oxide system towards NO-CO redox detoxification reaction. *Environ. Sci. Pollut. Res.* **2020**, *27*, 27061−27071.
(47) Fernández-García, M.; Martínez-Arias, A.; Belver, C.; Anderson, J. A.; Conesa, J. C.; Soria, J. Behavior of palladium−copper catalysts for CO and NO elimination. *J. Catal.* **2000**, *190*, 387−395.
(48) Jeon, J.; Kon, K.; Toyao, T.; Shimizu, K.; Furukawa, S. Design of Pd-based pseudo-binary alloy catalysts for highly active and selective NO reduction. *Chem. Sci.* **2019**, *10*, 4148−4162.
(49) Li, W.-J.; Wey, M.-Y. Dual immobilization of Pd−Cu nanoparticles on halloysite nanotubes by CTAB and PVP for automobile exhaust elimination. *Appl. Clay Sci.* **2021**, *214*, No. 106299.

(50) Xing, F.; Jeon, J.; Toyao, T.; Shimizu, K.-I.; Furukawa, S. A Cu−Pd single-atom alloy catalyst for highly efficient NO reduction. *Chem. Sci.* **2019**, *10*, 8292−8298.
(51) Iglesias-Juez, A.; Hungría, A. B.; Martínez-Arias, A.; Anderson, J. A.; Fernández-García, M. Pd-based (Ce,Zr)O_x-supported catalysts: promoting effect of base metals (Cr, Cu, Ni) in CO and NO elimination. *Catal. Today* **2009**, *143*, 195−202.
(52) Wu, Y.; Wang, Y.; Walter, E. D.; Rappé, K. G.; Wang, Y.; Gao, F. Insights into palladium poisoning of Cu/SSZ-13 selective catalytic reduction catalysts. *Appl. Catal. B Environ.* **2023**, *331*, No. 122673.
(53) Debauge, Y.; Abon, M.; Bertolini, J. C.; Massardier, J.; Rochefort, A. Synergistic alloying behaviour of $Pd_{50}Cu_{50}$ single crystals upon adsorption and co-adsorption of CO and NO. *Appl. Surf. Sci.* **1995**, *90*, 15−27.
(54) Li, J.-R.; Kuppler, R. J.; Zhou, H.-C. Selective gas adsorption and separation in metal-organic frameworks. *Chem. Soc. Rev.* **2009**, *38*, 1477−1504.
(55) Holles, J. H.; Davis, R. J.; Murray, T. M.; Howe, J. M. Effects of Pd particle size and ceria loading on NO reduction with CO. *J. Catal.* **2000**, *195*, 193−206.
(56) Chen, B.; Ma, Y.; Ding, L.; Xu, L.; Wu, Z.; Yuan, Q.; Huang, W. XPS and TPD study of NO interaction with Cu(111): role of different oxygen species. *Chin. J. Catal.* **2013**, *34*, 964−972.
(57) Rainer, D. R.; Vesecky, S. M.; Koranne, M.; Oh, W. S.; Goodman, D. W. The CO + NO reaction over Pd: a combined study using single-crystal, planar-model-supported, and high-surface-area Pd/Al_2O_3 catalysts. *J. Catal.* **1997**, *167*, 234−241.
(58) Hirsimäki, M.; Valden, M. Adsorption and thermal behavior of CO and NO on Pd{110} and Pd{320}. *J. Chem. Phys.* **2001**, *114*, 2345−2354.
(59) Baldanza, M. A. S.; de Mello, L. F.; Vannice, A.; Noronha, F. B.; Schmal, M. Adsorptive and catalytic properties of alumina-supported Pd−Mo catalysts. *J. Catal.* **2000**, *192*, 64−76.
(60) Ciuparu, D.; Bensalem, A.; Pfefferle, L. Pd−Ce interactions and adsorption properties of palladium-CO and NO TPD studies over $Pd-Ce/Al_2O_3$ catalysts. *Appl. Catal., B* **2000**, *26*, 241−255.
(61) Rochefort, A.; Fournier, R. Quantum chemical study of CO and NO bonding to Pd_2, Cu_2, and PdCu. *J. Phys. Chem.* **1996**, *100*, 13506−13513.
(62) Illas, F.; López, N.; Ricart, J. M.; Clotet, A.; Conesa, J. C.; Fernández-García, M. Interaction of CO and NO with PdCu(111) surfaces. *J. Phys. Chem. B* **1998**, *102*, 8017−8023.
(63) Kuroishi, K.; Fauzan, M. R. Al; Pham, T. N.; Wang, Y.; Hamamoto, Y.; Inagaki, K.; Shiotari, A.; Okuyama, H.; Hatta, S.; Aruga, T.; et al. A flat-lying dimer as a key intermediate in NO reduction on Cu(100). *Phys. Chem. Chem. Phys.* **2021**, *23*, 16880−16887.
(64) Al Fauzan, M. R.; Pham, T. N.; Halim, H. H.; Hamamoto, Y.; Inagaki, K.; Hamada, I.; Morikawa, Y. First-principles microkinetic study of NO reduction on Cu catalysts. *J. Phys. Chem. C* **2023**, *127*, 19451−19467.